Progress In Electromagnetics Research C, Vol. 172, 405–415, 2026

PIER C

(Received 12 July 2026, Accepted 2 August 2026, Scheduled 19 August 2026)

A Novel Funnel-Shaped High-Isolation MIMO Antenna for UWB Applications

Shanhua Yao, Yuting Wang*, Zhonggen Wang, and Han Lin

School of Electrical and Information Engineering, Anhui University of Science and Technology, Huainan 232001, China

ABSTRACT: This paper presents a compact, funnel-shaped, MIMO antenna for ultra-wideband (UWB) applications. The antenna element consists of a top funnel-shaped patch and a bottom rectangular ground plane. By using an elliptical slot on the patch and a slit at the center of the ground plane, impedance matching is effectively improved, and bandwidth is significantly expanded. Meanwhile, by etching a slot at the center of the ground plane and introducing semicircular slots and T-shaped parasitic stubs, mutual coupling between antenna elements is successfully suppressed. The overall dimension of the antenna is $48 \times 27 \times 1.6\,\text{mm}^3$. The simulated and measured results exhibit excellent agreement, demonstrating that the antenna achieves a continuous impedance bandwidth covering 3.16–16.48 GHz, which corresponds to a fractional bandwidth of 135.64%. Across the entire operating band, the port isolation exceeds 20 dB; the radiation efficiency ranges from 73.4% to 92.6%; the envelope correlation coefficient (ECC) is below 0.0025; and the diversity gain (DG) is better than 9.9982 dB. Combining ultra-wide bandwidth, high isolation, and extremely low channel correlation, the proposed antenna provides a reliable solution for high-performance UWB-MIMO communication systems.

1. INTRODUCTION

Ultra-wideband (UWB) systems play a vital role in modern wireless communication owing to their advantages, such as wide bandwidth, high transmission rates, and low power consumption [1, 2]. However, inherently restricted by their operational mechanisms and wireless propagation characteristics, UWB signals are highly susceptible to multipath effect, which easily induces signal distortion and deep fading, thereby degrading communication stability and transmission quality [3]. Furthermore, a single-antenna UWB architecture offers limited channel capacity, making it challenging to fully explore the potential of spectrum resources. To circumvent these limitations, researchers have combined UWB technology with multiple-input multiple-output (MIMO) technology [4], leading to the development of UWB-MIMO antenna technology [5]. This hybrid scheme effectively enhances channel capacity and data throughput while suppressing adverse effects of multipath fading, significantly optimizing overall communication performance [6, 7]. Nevertheless, because the element spacing in UWB-MIMO antennas is typically small, severe electromagnetic coupling between elements has become a critical bottleneck restricting overall system performance [8]. This bottleneck is not unique to UWB-MIMO systems; it is a long-standing common challenge in antenna engineering, as similarly observed in Yagi-Uda array designs in which gain and bandwidth cannot be simultaneously optimized without performance compromises [9].

Currently, state-of-the-art MIMO antenna decoupling techniques are broadly classified into two categories: self-decoupling and external decoupling structures. Self-decoupling techniques primarily rely on the antenna's geometric configuration to achieve high isolation, with common methods including orthogonal polarization layouts [10] and common-mode or differential-mode tuning method. Although self-decoupling approaches offer compact configurations without introducing additional losses, they are highly sensitive to frequency variations and are usually applicable only to narrowband environments. Consequently, for UWB systems with an extremely wide frequency span, self-decoupling struggles to maintain stable high isolation across the entire operating band. In contrast, external decoupling structures mitigate coupling discrepancies across different bands by incorporating auxiliary configurations, such as defected ground structures (DGS) [11], isolation stubs [12], neutralization lines [13], and lumped elements, thereby more effectively suppressing electromagnetic field coupling and surface-wave interference throughout the entire band [14]. This design paradigm of tailoring electromagnetic field distributions through structural reconfiguration for wideband performance enhancement has been extensively verified in array antenna optimization, as exemplified by clustered fractal arrays that achieve sidelobe suppression and directivity improvement while retaining their inherent multiband characteristics [15]. However, how to suppress inter-element coupling over an ultra-wide frequency spectrum while preserving favorable radiation performance — thereby fully unleashing diversity and spatial multiplexing advantages of MIMO systems — remains a core challenge in current UWB-MIMO antenna design [16].

To address these challenges, this paper proposes a compact, funnel-shaped UWB-MIMO antenna, featuring high isolation. To tackle decoupling difficulties across the entire UWB, a composite decoupling configuration consisting of semi-circular slots and a T-shaped stub is innovatively implemented. Via the effective reconfiguration of the surface current paths on the ground plane enabled by this structure, the electromagnetic mu-

* Corresponding author: Yuting Wang (2025200938@aust.edu.cn).

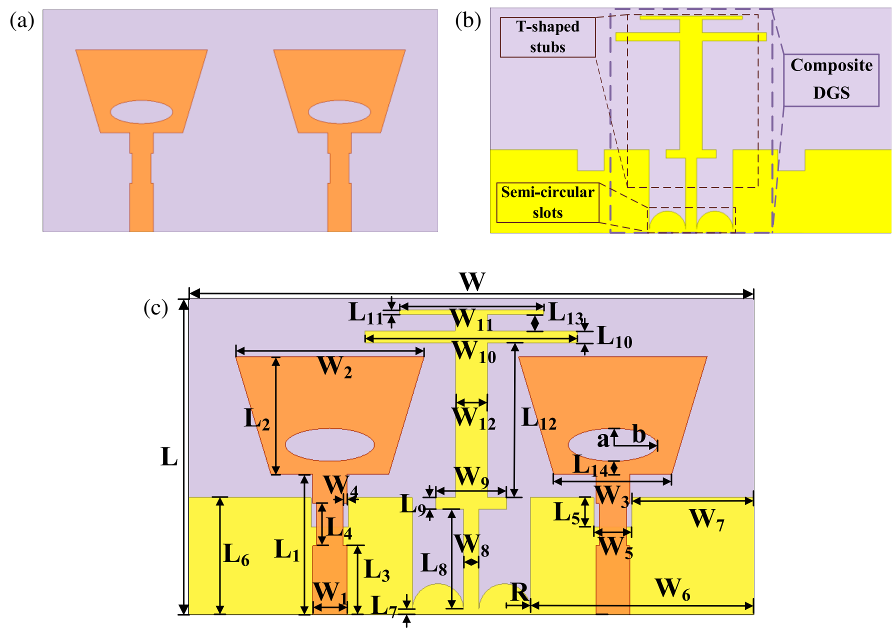

FIGURE 1. (a) Front view, (b) back view, and (c) structure and dimensions of the proposed antenna.

tual coupling between antenna elements is significantly mitigated. Both simulated and measured results demonstrate that the proposed antenna maintains a port isolation consistently below -20 dB across an ultra-wide operating frequency range of 3.16–16.48 GHz. Moreover, the antenna features a compact overall layout, preserving a distinct miniaturization advantage while sustaining excellent wideband radiation capabilities and diversity performance, thereby offering a novel and highly efficient solution for modern UWB-MIMO communication antenna designs.

2. ANTENNA DESIGN PROCESS

2.1. Antenna Geometry

The UWB-MIMO antenna proposed in this study is fabricated on a low-cost FR4 dielectric substrate with a relative permittivity of 4.4 and a loss tangent of 0.02, featuring a compact overall size of $48 \times 27 \times 1.6\,\text{mm}^3$. The detailed geometric configuration of the antenna is illustrated in Fig. 1. Its top layer, Fig. 1(a), consists of two side-by-side radiating elements, both fed by $50\,\Omega$ microstrip lines. The radiating elements employ a "funnel-shaped" patch topology, which evolves from a conventional rectangular main patch by symmetrically truncating two identical right-angled triangles from its left and right edges. To enhance isolation between antenna elements, a composite DGS is introduced into the bottom ground plane for decoupling, as depicted in Fig. 1(b). This composite DGS uses multiple decoupling mechanisms, including blocking conduction coupling, introducing reverse-field cancellation, and suppressing surface-wave propagation, thereby achieving high isolation for the UWB antenna across the entire operating band. The antenna's detailed geometric dimensions are annotated in Fig. 1(c). The structural parameters were optimized using electromagnetic simulation software, and the finalized dimensions are summarized in Table 1.

Simulated S-parameters of the proposed antenna are illustrated in Fig. 2. As observed, the S_{11} parameter maintains continuous and stable impedance-matching characteristics across a wide frequency range of 3.16–16.48 GHz, fully satisfying the UWB standard requirements. Furthermore, mutual coupling between antenna elements is effectively suppressed, with the port isolation (S_{12} parameter) remaining below -20 dB throughout the entire operating band. This excellent decoupling performance effectively ensures the reliability of the UWB-MIMO system in high-speed data transmission applications.

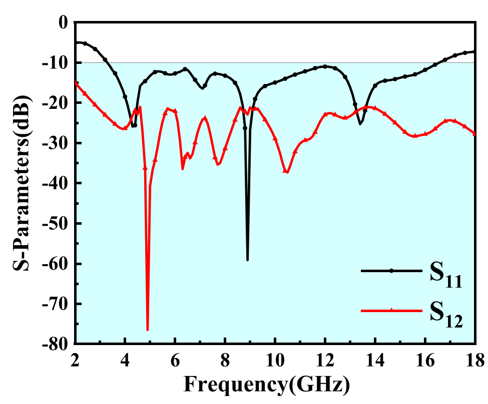

FIGURE 2. The S-parameters of the proposed antenna.

2.2. Proposed Single Antenna Evolution

Figure 3(a) illustrates the structural evolution of the proposed UWB monopole antenna. The S_{11} and Smith charts for each evolutionary stage are depicted in Figs. 3(b) and 3(c), respectively. The initial design, designated as Ant 1, consists of a front rectangular patch, a feedline integrated with a quarter-wavelength impedance transformer, and a solid rectangular ground plane on the back. As shown in Fig. 3(b), its impedance bandwidth for S_{11} less than -10 dB spans only from 3.3 to

TABLE 1. Optimized dimensions of antenna parameters.

Parameter	L	L_1	L_2	L_3	L_4	L_5	L_6	L_7	L_8
Size (mm)	27	12	10	5.9	3.6	2.5	10	0.5	8.5
Parameter	L_9	L_{10}	L_{11}	L_{12}	L_{13}	L_{14}	W	W_1	W_2
Size (mm)	1	1	0.4	13	1.6	1	48	2.88	16
Parameter	W_3	W_4	W_5	W_6	W_7	W_8	W_9	W_{10}	W_{11}
Size (mm)	10	0.35	3.2	19	10.4	1.3	6	18	12.24
Parameter	W_{12}	a	b	R					
Size (mm)	2.7	1.4	3.78	2.175					

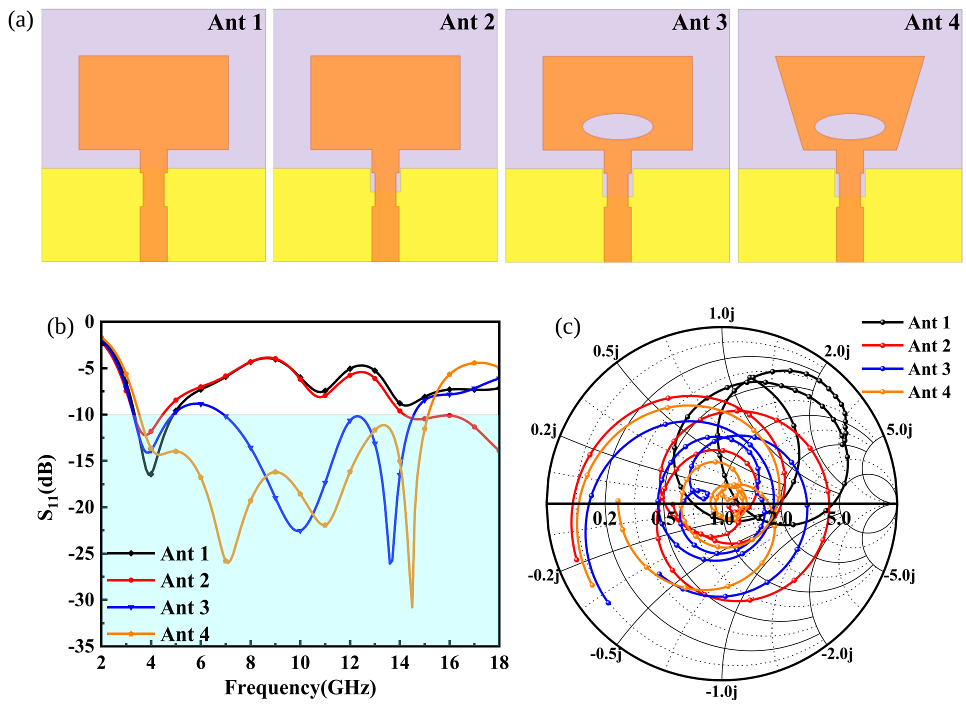

FIGURE 3. (a) Structural evolution of monopole antennas, (b) S_{11}, and (c) Smith chart.

4.9 GHz, which falls far short of the requirements for UWB operation. The Smith chart in Fig. 3(c) reveals that most of the impedance trajectory in this frequency range is in the upper-right quadrant, exhibiting high resistance and high inductance. To extend operating bandwidth, it is essential to guide the impedance trajectory toward the center of the normalized Smith chart (1.0). To this end, Ant 2 is developed by introducing a rectangular slot into the rear ground plane of Ant 1, thereby forming a DGS. This modification introduces a series capacitance into the equivalent circuit, effectively counteracting the excessive inductive component of the original antenna. Consequently, the impedance trajectory across the entire band shifts toward the lower-left region of the Smith chart. On the S_{11} curve, this is manifested as the excitation of a new resonance band at the higher frequencies from 13.0 to 16.6 GHz. Further inspection of the Smith chart indicates that the frequency band around 10 GHz remains in a high-resistance state. To address this, Ant 3 is constructed by etching an elliptical slot in the center of the rectangular patch of Ant 2 to introduce capacitive loading. This modification successfully generates a new resonance point near 10 GHz, thereby further broadening the impedance bandwidth. Nevertheless, the Smith chart reveals that impedance trajectories for certain frequency segments still deviate significantly from the normalized origin. To further optimize the impedance matching, Ant 4 is evolved by introducing beveled corners to the rectangular patch of Ant 3. This approach successfully modifies the surface current distribution, enabling a smoother transition of the current from the feedline to the radiating patch. Ultimately, Ant 4 achieves a UWB operating frequency range 3.5 to 15.2 GHz with significantly enhanced impedance-matching performance.

2.3. Decoupling Design of the MIMO Antenna

To further enhance the antenna's reliability, signal quality, and data transmission rate, this section discusses the development of dual-port MIMO antennas. The single-pole UWB antenna proposed in Section 2 is arranged in parallel and forms the initial dual-port design, called $MIMO_1$. Its structure is shown in Fig. 4(a). Fig. 4 illustrates the structural comparison and the

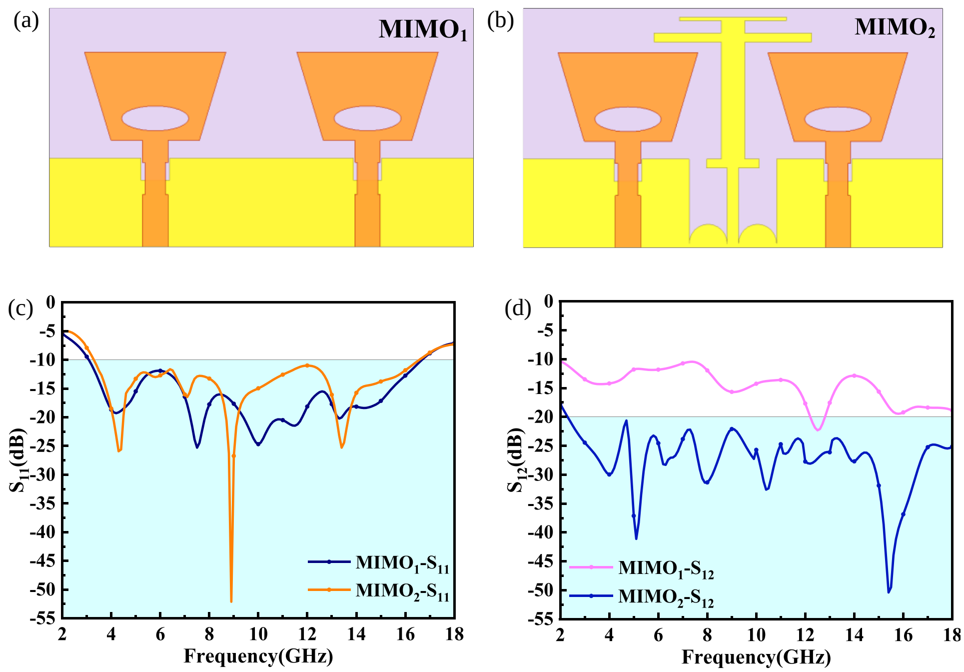

FIGURE 4. (a) MIMO_1, (b) MIMO_2, (c) S_{11} parameters, and (d) Isolation parameters.

corresponding S-parameters of the MIMO antenna before and after integrating the isolation structure.

Figure 4 shows the structural comparison of the two MIMO antennas before and after the decoupling isolation structure is loaded, as well as the corresponding S-parameter characteristic curves. The reference antenna (MIMO_1) without a decoupling structure has poor port isolation, with an isolation superior to 20 dB only in a narrow band from 12.15 to 13.06 GHz. The isolation level in other frequency bands fails to meet the design requirements. To achieve an isolation improvement across the entire working frequency range, a composite decoupling structure consisting of semi-circular slots and T-shaped stubs is introduced based on the structure of MIMO_1. This design effectively blocks the propagation path of surface-wave current along the ground plane. Although near-field coupling between decoupling elements and the radiation patch can excite additional resonant modes, causing fluctuations in the S_{11} curve, the antenna's return loss is below 10 dB throughout the entire working frequency range of 3.16 to 16.48 GHz, and the UWB working characteristics are not significantly affected. The MIMO_2 antenna after loading the composite decoupling structure has significantly suppressed the S_{12} isolation between ports, and the coupling strength of each unit in the entire working frequency range is lower than -20 dB. This improvement effectively addresses the isolation deficiency of the original antenna and verifies the excellent performance of the proposed composite decoupling structure in suppressing unit mutual coupling and enhancing the anti-interference ability of MIMO antennas in complex electromagnetic environments.

2.4. Equivalent Circuit Analysis

To gain deeper insight into the operating mechanism of the proposed antenna, an equivalent circuit model was constructed using Advanced Design System (ADS). Fig. 5(a) illustrates the complete equivalent circuit topology, with its corresponding lumped component values listed in Table 2. Figs. 5(b) and 5(c) depict the simulated and equivalent circuit S_{11} responses for the single element (Ant 4) and the MIMO configuration, respectively. As shown in Fig. 5(a), the feed line section is modeled by a series C_p-L_p and a parallel C_1-L_1 resonant network to account for the discontinuity effects of the SMA connector and transmission lines. The resonator block, composed of four parallel RLC resonant networks, is employed to characterize the antenna's four primary resonant modes. Considering the complex spatial electromagnetic coupling between adjacent antenna elements, a parallel LC decoupling network (L_c and C_c) is incorporated into the equivalent-circuit model to characterize mutual coupling effects. The comparison demonstrates good agreement between the circuit model and full-wave electromagnetic simulation. The slight discrepancy is mainly attributed to the inherent differences between the distributed-parameter nature of the physical antenna and the lumped-parameter implementation of the circuit model, as well as the unmodeled dielectric losses from the substrate and high-frequency radiation losses along the transmission lines.

TABLE 2. Parameters of the equivalent circuit (Units: *Resistance* in Ω, *Capacitance* in pF, *Inductance* in nH).

Parameter	Value	Parameter	Value	Parameter	Value
C_1	0.059	L_1	5.975	R_1	49.72
C_2	0.410	L_2	0.571	R_2	74.71
C_3	0.847	L_3	1.457	R_3	43.58
C_4	2.991	L_4	0.041	R_4	413.36
C_5	3.013	L_5	9.759	L_c	0.361
C_p	1.044	L_p	0.737	C_c	1.914

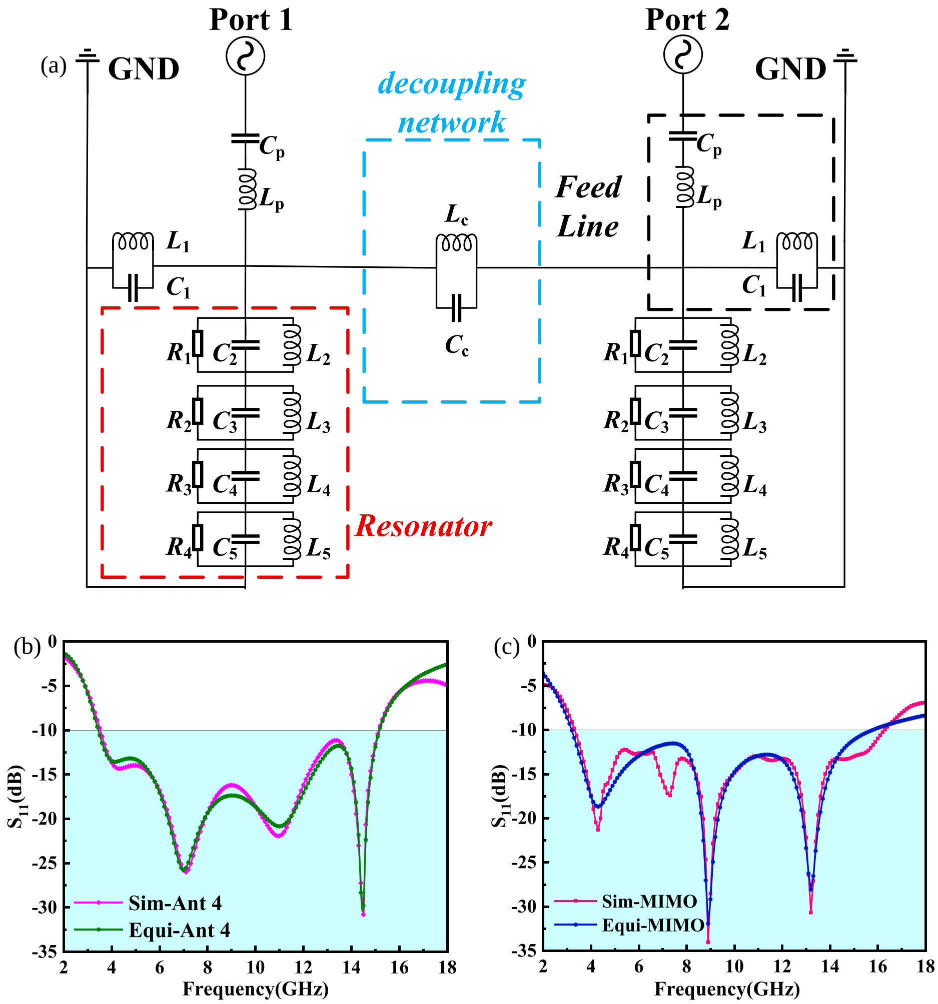

FIGURE 5. Equivalent circuit and corresponding S-parameters: (a) Equivalent circuit; (b) and (c) S_{11} parameters.

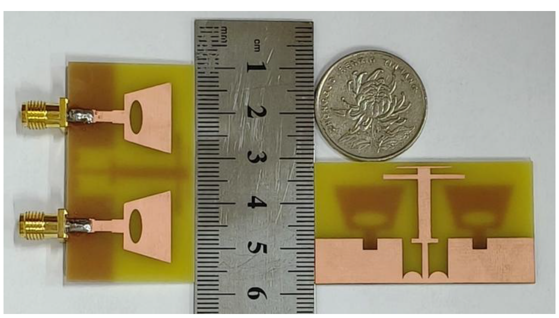

FIGURE 6. Photograph of the fabricated physical antenna.

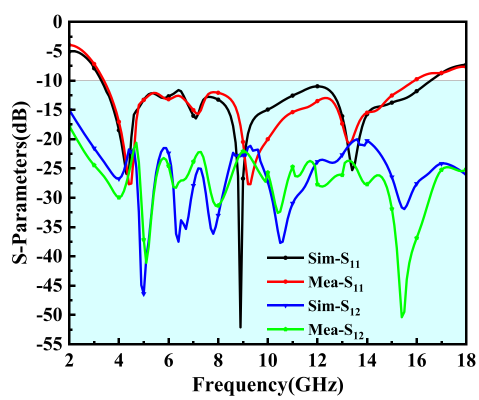

FIGURE 7. Comparison of simulated and measured S-parameters.

3. ANTENNA PERFORMANCE ANALYSIS

3.1. Simulated and Measured S-Parameters

To verify the feasibility of the proposed antenna, after completing the simulation and optimization, the proposed UWB-MIMO antenna was fabricated. Fig. 6 shows a photo of the fabricated antenna, and Fig. 7 presents the comparison between measured S parameters by the vector network analyzer (VNA) and simulation results.

From the test results, it can be seen that the measured S_{11} curve within the entire working frequency band maintains good consistency with the simulation trend; it can be observed that the measured S_{11} parameter at the resonant point is slightly less than the simulation value, which is mainly attributed to manufacturing tolerances, welding effect of the SMA connector, and minor fluctuations in dielectric substrate parameters, but it still meets requirements of UWB performance within the fre-

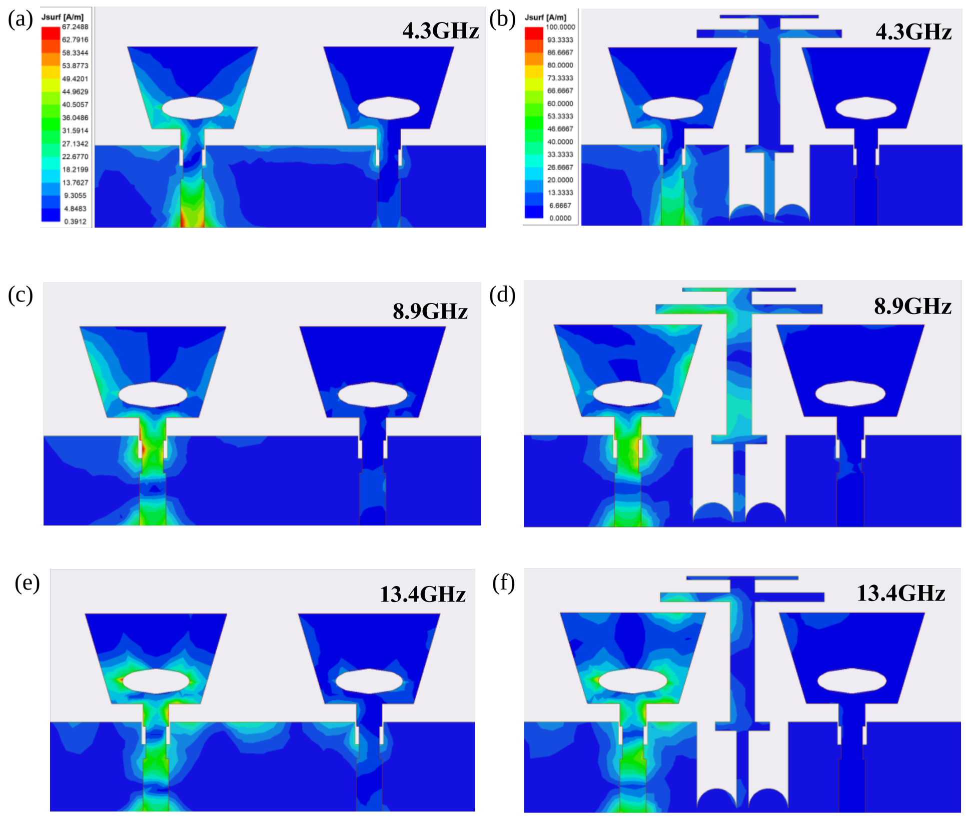

FIGURE 8. Surface current distributions of the antenna at different frequencies: (a), (c), (e) without the decoupling structure; (b), (d), (f) with the decoupling structure.

quency band. This fully verifies the antenna's excellent wideband impedance-matching performance. At the same time, the measured isolation parameter S_{12} shows good agreement with the simulation data and remains above 20 dB throughout the frequency band. The above results indicate that the composite decoupling structure, composed of semi-circular slots and T-shaped branches, has robustness, can effectively suppress performance degradation caused by processing errors, ensure excellent electromagnetic isolation between antenna units, and meet the application requirements of high-performance UWB-MIMO communication systems.

3.2. Antenna Current Analysis

To elucidate the operating mechanism of the composite decoupling structure composed of semicircular slots and T-shaped stubs, this paper further analyzes the antenna's surface current distribution. Fig. 8 presents the surface current distributions at three typical resonant frequencies (4.3 GHz, 8.9 GHz, and 13.4 GHz), with and without the decoupling structure. All results are acquired under the condition that the left port is excited while the right port is terminated with a 50 Ω load. As observed in Figs. 8(a), 8(c) and 8(e), in the absence of the decoupling structure, intense coupling current propagates from the microstrip feed line of the left port to the adjacent right port via the ground plane, resulting in deteriorated port isolation. The isolation level at 4.3 GHz and 8.9 GHz is merely approximately 15 dB. With the proposed composite decoupling structure loaded, as illustrated in Figs. 8(b), 8(d), and 8(f), most of the coupled current is concentrated around the decoupling structure composed of T-shaped stubs and semi-circular slots. The current amplitude at the right port is significantly attenuated, thereby greatly improving port isolation. The comparative results of surface current distributions corroborate the improvement in isolation performance, fully validating the decoupling effectiveness of the semicircular-slot and T-shaped-stub composite structure for UWB-MIMO antennas.

To further clarify physical decoupling mechanisms, Fig. 9 compares vector current distributions at 4.9 GHz and 10.5 GHz. For MIMO_1 (without decoupling), strong vector currents flow directly across the continuous ground plane to the adjacent port. For MIMO_2, the composite structure dramatically alters current paths. At 4.9 GHz: The semi-circular slots block the direct conducted currents, while the central T-shaped stubs induce localized reverse currents that generate opposing fields to suppress the mutual coupling. At 10.5 GHz: The slotted ground pattern acts as a high-impedance barrier, effectively trapping high-frequency energy within decoupling branches and suppressing surface-wave propagation. Consequently, the current amplitude at the right port is dramatically attenuated, validating the effectiveness of conduction-path interruption, reverse-field cancellation, and surface-wave containment.

3.3. Envelope Correlation Coefficient and Diversity Gain

As a core metric for evaluating diversity characteristics of MIMO systems, the envelope correlation coefficient (ECC) characterizes the degree of statistical decorrelation among the

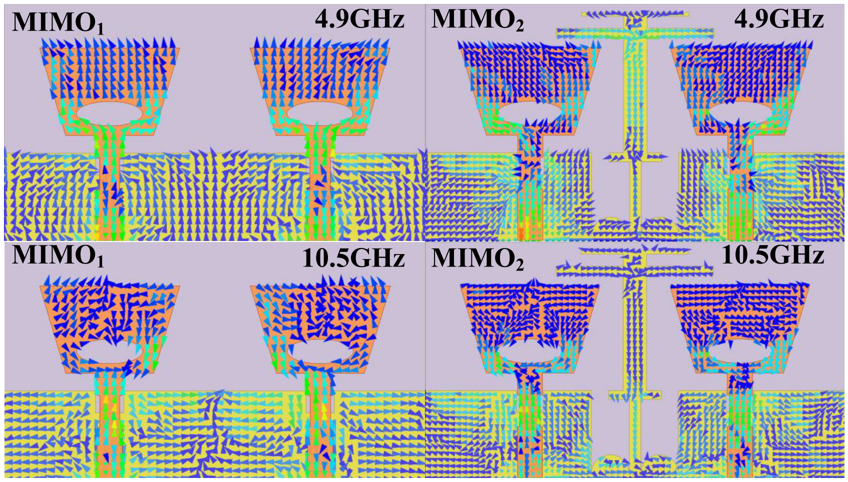

FIGURE 9. Vector current distributions of the antenna at different frequencies.

signals received by individual antenna elements in a multipath channel. From the perspective of electromagnetic field theory, the ECC primarily reflects the overlap probability of the pattern functions and polarization waveforms of different radiating branches in free space, with a threshold of ECC < 0.5 universally adopted as a strict criterion to ensure sufficient channel independence. In terms of characterization methodologies, although the algebraic algorithm based on the scattering matrix (S-parameters) is widely accepted due to its high computational efficiency, it often fails to fully map the authentic free-space radiation status for UWB systems that frequently incorporate complex near-field passive decoupling networks. In contrast, the solid-angle full-integration method based on three-dimensional (3D) far-field radiation patterns can comprehensively capture the polarization vectors, phase gradients, and energy distributions of each radiating element in space, thereby serving as the most intrinsic and high-fidelity approach to quantifying spatial diversity performance. When ECC approaches its theoretical limit of zero, the respective channel matrices become mutually independent, driving the system into an ideal state of electromagnetic decoupling. Under this condition, even if a specific branch undergoes destructive deep fading during multipath transmission, the remaining uncorrelated spatial channels can still construct a robust signal barrier, thereby endowing the entire MIMO architecture with an excellent fading margin and substantial diversity gain. This low-interference environment fully unleashes the spatial multiplexing potential, fundamentally safeguarding the topological robustness of the communication link under high-speed, high-capacity data transmission and suppressing the bit error rate (BER) to an extremely low level. Based on the 3D far-field radiation field vectors, the ECC calculation model for a MIMO system can be formulated as follows:

$$\mathrm{ECC}=\frac{\left|S_{11}^{*}S_{12}+S_{21}^{*}S_{22}\right|^{2}}{\left(1-\left|S_{11}\right|^{2}-\left|S_{21}\right|^{2}\right)\left(1-\left|S_{22}\right|^{2}-\left|S_{12}\right|^{2}\right)} \tag{1}$$

$$\mathrm{ECC}=\frac{\left|\int_{\Omega}E_{1}(\theta,\varphi)\times E_{2}^{*}(\theta,\varphi)d\Omega\right|^{2}}{\int_{\Omega}\left|E_{1}(\theta,\varphi)\right|^{2}d\Omega\times\int_{\Omega}\left|E_{2}(\theta,\varphi)\right|^{2}d\Omega} \tag{2}$$

As a core metric for evaluating the leap in link reliability of multi-antenna systems, diversity gain (DG) inherently characterizes the degree of improvement in statistical certainty of the received signal enabled by spatial diversity techniques. In terms of physical mechanisms, the essence of DG lies in the spatial synthesis of multiple independent fading channels, which effectively smooths the fluctuations in the instantaneous signal-to-noise ratio (SNR) of the composite received signal, thereby constructing a robust barrier against large-scale fading. The depth to which this gain is released depends entirely on spatial decorrelation characteristics of the channel matrix. In propagation environments rich in multipath scattering, the field strength envelopes captured by individual radiating elements exhibit highly uncorrelated fading, which provides the fundamental electromagnetic prerequisite for diversity algorithms to extract energy redundancy in the spatial domain. Conversely, without the physical support of complex scattering environments, joint probability distributions among the channels tend to degenerate, causing the diversity gain to encounter an insurmountable theoretical upper limit at the physical layer. Consequently, the outstanding diversity gain not only directly reflects the enhanced robustness of the communication link topology, but also profoundly demonstrates the inherent advantages of the MIMO architecture in utilizing spatial degrees of freedom to mitigate the effects of channel fading. Within the quantitative framework of microwave engineering, the numerical value of DG is typically derived as the ECC's mapping function, and their mathematical logical relationship can be formulated as follows:

$$\mathrm{DG}=10\sqrt{1-\mathrm{ECC}^{2}} \tag{3}$$

Figure 10 presents the simulated ECC and DG results of the proposed MIMO antenna calculated using both port scattering parameters and 3D far-field radiation patterns across the operating band. Specifically, as shown in Fig. 10(a), the port-based ECC remains below 0.005 within the 3.16–16.48 GHz UWB range, while the corresponding port-based DG stabilizes above 9.972 dB, nearing the theoretical limit of 10 dB. In contrast, the far-field-based results derived from solid-angle integration are illustrated in Fig. 10(b), yielding a peak far-field ECC of 0.068

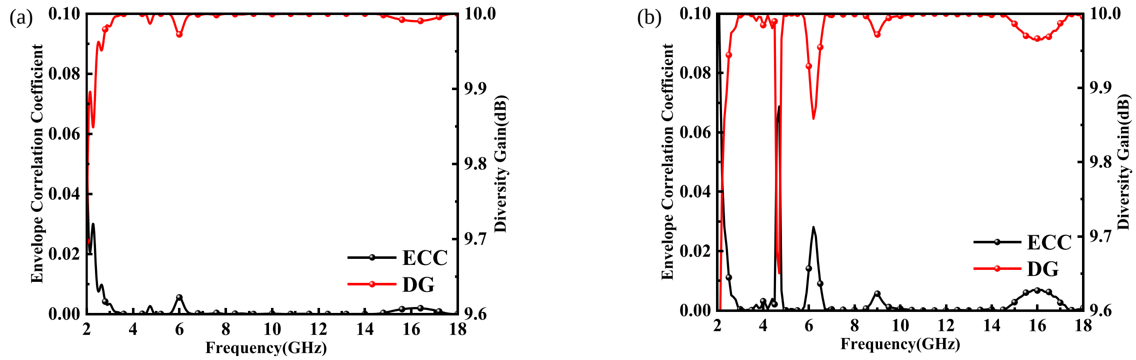

FIGURE 10. Simulated ECC and DG: (a) S-parameters and (b) far-field radiation patterns.

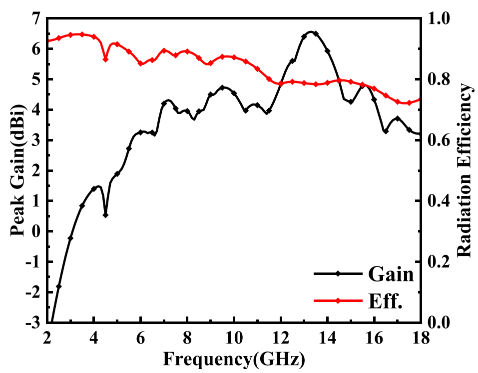

FIGURE 11. Antenna peak gain and radiation efficiency.

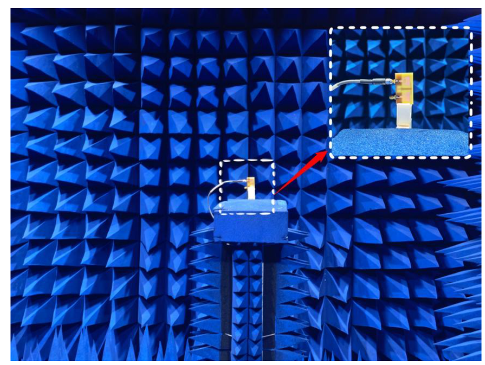

FIGURE 12. Measured in a microwave anechoic chamber.

and a far-field DG greater than 9.650 dB across the entire spectrum. This slight numerical variation in the far-field metrics is primarily attributed to the inclusion of spatial cross-polarization coupling and the near-field surface-wave reradiation induced by the lossy FR4 substrate. Nevertheless, both evaluation methods yield ECC values well below the 0.5 threshold along with outstanding DG performance, demonstrating that the composite decoupling structure consisting of semi-circular slots and a T-shaped stub successfully suppresses mutual coupling and achieves strong spatial channel decorrelation.

3.4. Antenna Peak Gain and Efficiency

Figure 11 depicts the simulated radiation efficiency and far-field peak gain trends of the proposed UWB-MIMO antenna. The data indicate that the simulated radiation efficiency of the system remains within a high-level range of 72.1%–94.2% across the entire operating band. Despite the selection of a low-cost FR4 substrate with relatively large dissipation, the antenna still maintains a highly efficient radiation output. Additionally, the simulated peak gain of the antenna ranges from -0.53 dBi to 6.53 dBi. The gain exhibits a noticeable upward trend accompanied by minor fluctuations in the high-frequency band, which is primarily attributed to the relative increase in the radiator's electrical size as the operating frequency rises, thereby enhancing the antenna's directivity.

3.5. Radiation Performance Analysis of the Antenna

Figure 12 shows the schematic diagram of the physical far-field test device of the antenna in a microwave anechoic chamber.

Figure 13 compares simulation results in XOY and XOZ planes of this MIMO antenna in three typical resonant frequencies (4.3 GHz, 8.9 GHz, and 13.4 GHz), as well as the measured two-dimensional radiation patterns. From the figure, it can be seen that the simulated and measured results are in good agreement in all frequency bands, verifying the correctness of the antenna design. At the low-frequency band of 4.3 GHz, the antenna exhibits a significant asymmetric directional radiation characteristic. Due to the only left port 1 feeding, the surface current distribution breaks the geometric symmetry, causing the main lobe to shift significantly to one side; at this time, strong directional selectivity is shown on the XOZ plane, while the non-fed side shows obvious energy attenuation and biased depression. As the operating frequency increases to 8.9 GHz, the antenna size increases, and the direction pattern begins to show a multi-lobe tendency. The main lobe widens, and a more obvious side lobe is excited in the non-fed unit direction. This is mainly due to high-order electromagnetic coupling among the feeding unit, intermediate decoupling structure, and adjacent units at high frequencies, which causes the omnidirectional or wide-beam radiation characteristic of the XOY plane to be distorted by the asymmetric current. When the operating frequency reaches the high-frequency band of 13.4 GHz, the surface-current distribution of the antenna becomes more complex, and high-order modes are strongly excited, resulting in significant split lobes and asymmetric multi-lobe characteristics on both XOZ and XOY planes. The spatial energy distribution becomes more scattered. This asymmetric radiation characteristic on the XOZ and XOY planes under single-port feeding makes the direction pattern of port 2 mirror-symmetric

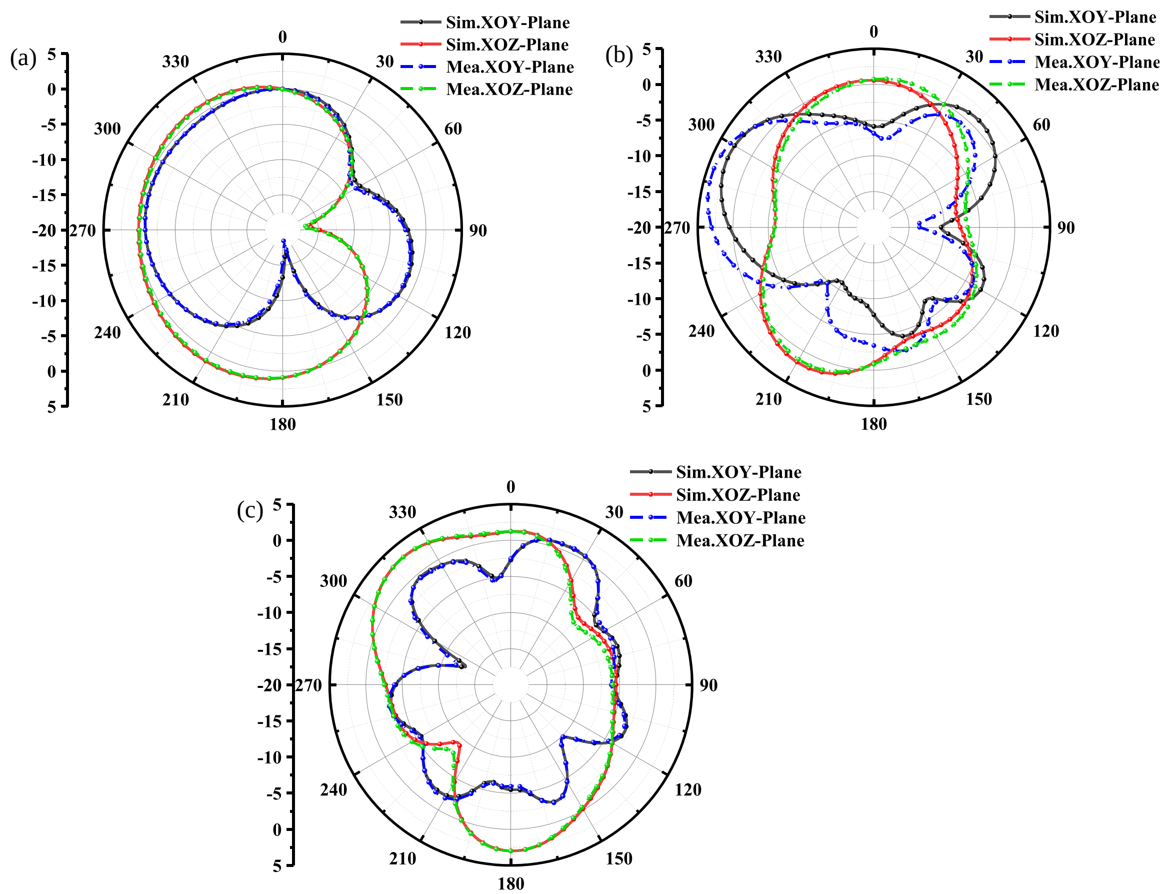

FIGURE 13. Simulated and measured orientation diagrams: (a) 4.3 GHz, (b) 8.9 GHz, and (c) 13.4 GHz.

when fed alone, and this characteristic can effectively reduce the ECC between ports, thereby significantly improving the fading resistance of this MIMO antenna system in multipath transmission environments.

3.6. Total Active Reflection Coefficient and Channel Capacity Loss

Given that the individual sub-elements of a MIMO antenna system operate with multi-port concurrent excitation in practical scenarios, the conventional isolated S-parameters have inherent limitations in fully characterizing the system's overall radiation and matching performance. Consequently, the quantitative evaluation of the system's total active reflection coefficient (TARC) has become an indispensable, critical phase in multi-antenna design. As a matrix-level energy metric, TARC can faithfully capture the overall net reflected power across multiple channels under any arbitrary, random excitation phase stream. Within the framework of microwave engineering computations, this index is typically derived analytically as a function of the port scattering matrix, and its standard algebraic formulation is expressed as follows:

$$\text{TARC} = \sqrt{\frac{\left|S_{11} + S_{12}e^{j\theta}\right|^2 + \left|S_{21} + S_{22}e^{j\theta}\right|^2}{2}} \tag{4}$$

As one of the core performance metrics in multi-antenna design, channel capacity loss (CCL) aims to quantify the negative physical degradation inflicted on the ideal channel transmission rate by imperfect decoupling between antenna elements. Within the paradigm of microwave engineering practices, a threshold of CCL < 0.4 bit/s/Hz is universally recognized as the critical technical benchmark to determine whether a MIMO antenna system fully complies with design specifications and is approved for commercial deployment. The quantitative derivation of this index fundamentally depends on the characteristic energy distribution of individual channels, and its standard algebraic computation model can be formulated as follows:

$$\text{CCL} = -\log_2 \det \left|\psi^R\right| \tag{5}$$

$$\psi^R = \begin{pmatrix} \rho_{11} & \dots & \rho_{1n} \\ \vdots & \ddots & \vdots \\ \rho_{m1} & \cdots & \rho_{mn} \end{pmatrix} \tag{6}$$

Figure 14(a) presents simulated TARC results of the proposed MIMO antenna under different relative excitation phase shifts ($\theta = 0°$, 90°, 180°, and 270°). Evidently, the TARC of the antenna remains below -10 dB across the entire targeted frequency band with all excitation phase combinations. Due to the outstanding decoupling characteristics and spatial symmetry of the MIMO structure, variations in individual input phases do not induce severe distortions in the TARC curves, with the overall trend of a highly compact distribution. This quantitatively demonstrates that the design has robust immunity to

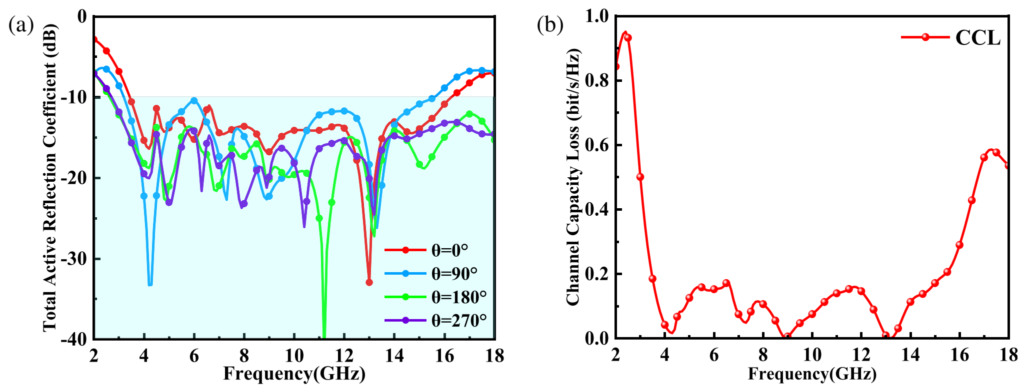

FIGURE 14. MIMO antenna system performance curves: (a) TARC and (b) CCL.

TABLE 3. Comparison of the proposed antenna with several existing antennas.

Ref.	Size(mm^2)	Bandwidth (GHz)	Port	Isolation (dB)	ECC	Gain (dBi)
[10]	22 × 26	3.1–10.6	2	> 18	< 0.004	3.8
[14]	50 × 30	4.66–15.97	4	> 20	< 0.035	7.83
[16]	25 × 36	2.74–14.8	2	> 20	< 0.005	5.4
[17]	50 × 29	2.4–11	2	> 18	< 0.04	2
[18]	40 × 40	3.82–15.9	2	> 17	< 0.005	6.33
[19]	30 × 45	5.8–10	2	> 15	/	4
[20]	55 × 55	3.15–20	4	> 15	< 0.008	6.13
[21]	55 × 55	2–16.49	4	> 16	< 0.24	6.72
This work	**27 × 48**	**3.16–16.48**	**2**	**> 20**	**< 0.0025**	**6.53**

multi-channel random-phase streams, providing extremely reliable and stable broadband impedance matching in actual multipath environments.

Figure 14(b) depicts the simulated CCL curve of the proposed MIMO antenna system. The results indicate that the CCL remains at an exceptionally low level within the core UWB operating band of 3.16–16.48 GHz. Although an upward trend is observed near the lower-frequency boundary and upper cutoff edge due to the gradual degradation of impedance matching and port isolation, the maximum in-band peak is strictly confined to 0.398 bit/s/Hz. This maximum value is well below the industrial design criterion of 0.4 bit/s/Hz, forcefully verifying that the antenna possesses excellent data throughput capabilities and high-efficiency information transmission quality across the entire designated spectrum.

Table 3 compares the performance of the proposed antenna with state-of-the-art designs. The results highlight several critical advantages of the proposed structure. Featuring a UWB response of 3.16–16.48 GHz, it delivers wider spectral coverage than most comparable designs. Crucially, the design exhibits excellent decoupling characteristics, achieving a port isolation exceeding 20 dB and an exceptionally low ECC below 0.0025. This minimized ECC confirms strong radiation decorrelation, effectively enhancing channel capacity and diversity performance. In terms of radiation performance, the antenna's simulated peak gain ranges from −0.53 dBi to 6.53 dBi, across the entire operating band. The gain exhibits an overall noticeable upward trend with frequency, delivering a competitive peak gain performance. Furthermore, compared to existing multi-port wideband solutions, the antenna achieves a more competitive, compact physical footprint (27 mm × 48 mm) without compromising electromagnetic performance. Overall, the proposed design offers an optimized trade-off among wideband operation, high isolation, and miniaturization, underscoring its high potential for practical MIMO engineering applications.

4. CONCLUSION

A compact, funnel-shaped UWB-MIMO antenna has been successfully designed, fabricated, and validated. By introducing semi-circular slots and T-shaped stubs into ground planes, a highly effective decoupling mechanism is established, successfully suppressing port isolation to below −20 dB. This proposed design overcomes the challenge of achieving high isolation in shared-ground systems across an ultra-wide frequency range. Experimental results indicate that the antenna provides stable operation from 3.16 to 16.48 GHz. Notably, the proposed design achieves a port isolation exceeding 20 dB and an ECC below 0.0025, which significantly surpass those of existing state-of-the-art designs. The high degree of consistency between the simulated and measured results further confirms the robustness of the proposed scheme. In summary, the antenna achieves an optimal balance among miniaturization, wideband characteristics, and decoupling performance, demonstrating substantial potential for future high-capacity and high-speed wireless applications.

ACKNOWLEDGEMENT

This work was supported in part by the International Joint Research Center for Intelligent Sensing and High-Dimensional Modeling of Ancient Buildings in Anhui Province under No. GJZZX2025KF03.

REFERENCES

[1] Sharbati, V., X. Bao, J. J. Healy, N. Zhang, K. Nadali, and M. J. Ammann, "Dynamic tuning of notch bands in UWB antenna based on liquid metal for cognitive radio applications," *IEEE Antennas and Wireless Propagation Letters*, Vol. 23, No. 12, 4708–4712, 2024.

[2] Nejdi, I. H., M. Marzouk, M. A. Lafkih, S. Bri, J. A. Nasir, Z. Zakaria, and A. J. A. Al-Gburi, "A low-profile UWB monopole antenna and high-isolated UWB-MIMO antenna for wireless communications networks," *Progress In Electromagnetics Research C*, Vol. 161, 105–119, 2025.

[3] Jayant, S., G. Srivastava, and S. Kumar, "Quad-port UWB MIMO footwear antenna for wearable applications," *IEEE Transactions on Antennas and Propagation*, Vol. 70, No. 9, 7905–7913, 2022.

[4] Nie, L. Y., X. Q. Lin, Z. Q. Yang, J. Zhang, and B. Wang, "Structure-shared planar UWB MIMO antenna with high isolation for mobile platform," *IEEE Transactions on Antennas and Propagation*, Vol. 67, No. 4, 2735–2738, 2019.

[5] Jayant, S. and G. Srivastava, "Close-packed quad-element triple-band-notched UWB MIMO antenna with upgrading capability," *IEEE Transactions on Antennas and Propagation*, Vol. 71, No. 1, 353–360, 2023.

[6] El Atrash, M., M. S. Khalil, W. A. Mahmoud, and M. A. Addalla, "A low-profile fully-fabric high isolation dual-port MIMO antenna for UWB wearable applications," *IEEE Transactions on Antennas and Propagation*, Vol. 74, No. 5, 3971–3979, 2026.

[7] Li, W., L. Wu, S. Li, X. Cao, and B. Yang, "Bandwidth enhancement and isolation improvement in compact UWB-MIMO antenna assisted by characteristic mode analysis," *IEEE Access*, Vol. 12, 17 152–17 163, 2024.

[8] Nie, L. Y., X. Q. Lin, S. Xiang, B. Wang, L. Xiao, and J. Y. Ye, "High-isolation two-port UWB antenna based on shared structure," *IEEE Transactions on Antennas and Propagation*, Vol. 68, No. 12, 8186–8191, 2020.

[9] Mohammed, J. R., "Design of printed Yagi antenna with additional driven element for WLAN applications," *Progress In Electromagnetics Research C*, Vol. 37, 67–81, 2013.

[10] Luo, C.-M., J.-S. Hong, and L.-L. Zhong, "Isolation enhancement of a very compact UWB-MIMO slot antenna with two defected ground structures," *IEEE Antennas and Wireless Propagation Letters*, Vol. 14, 1766–1769, 2015.

[11] Iqbal, A., O. A. Saraereh, A. W. Ahmad, and S. Bashir, "Mutual coupling reduction using F-shaped stubs in UWB-MIMO antenna," *IEEE Access*, Vol. 6, 2755–2759, 2018.

[12] Chen, Z., W. Zhou, and J. Hong, "A miniaturized MIMO antenna with triple band-notched characteristics for UWB applications," *IEEE Access*, Vol. 9, 63 646–63 655, 2021.

[13] Zhang, S. and G. F. Pedersen, "Mutual coupling reduction for UWB MIMO antennas with a wideband neutralization line," *IEEE Antennas and Wireless Propagation Letters*, Vol. 15, 166–169, 2016.

[14] Zheng, X., L. Yue, and Y. Zhang, "A compact four-port axially symmetric UWB-MIMO antenna array: Metamaterial-integrated coplanar waveguide for broadband operation with high isolation," *Progress In Electromagnetics Research C*, Vol. 162, 58–69, 2025.

[15] Mohammed, J. R. and D. A. Al-Khafaf, "Optimizing performance of antenna arrays with clustered fractal shapes for multiband applications," *Journal of Telecommunications and Information Technology*, Vol. 95, No. 1, 91–96, 2024.

[16] Wang, Z., G. Song, W. Nie, M. Yang, C. Li, and M. Wang, "A racket-like UWB MIMO antenna with high isolation," *Progress In Electromagnetics Research C*, Vol. 144, 159–168, 2024.

[17] Potti, D., Y. Tusharika, M. G. N. Alsath, S. Kirubaveni, M. Kanagasabai, R. Sankararajan, S. Narendhiran, and P. B. Bhargav, "A novel optically transparent UWB antenna for automotive MIMO communications," *IEEE Transactions on Antennas and Propagation*, Vol. 69, No. 7, 3821–3828, 2021.

[18] Rajesh, G. and R. Poonkuzhali, "Design and analysis of CPW fed ultrathin flexible MIMO antenna for UWB and X-band applications," *IEEE Access*, Vol. 12, 96 704–96 717, 2024.

[19] Mazzinghi, A., D. Barras, B. Danev, and A. Freni, "Miniaturized UWB dual-port antenna for localization applications," *IEEE Antennas and Wireless Propagation Letters*, Vol. 23, No. 3, 1080–1084, 2024.

[20] Kamal, M. M., B. Wang, N. Shoaib, U. Rafique, M. I. Abbasi, and M. R. Kamarudin, "Self-decoupled quad-port CPW-fed fractal MIMO antenna with UWB characteristics," *International Journal of Antennas and Propagation*, Vol. 2024, No. 1, 3826899, 2024.

[21] Srivastava, G., M. Al-Hamami, S. Kumar, O. P. Kumar, *et al.*, "Triple-band notched and highly decoupled MIMO antenna using characteristic mode analysis," *IEEE Access*, Vol. 13, 165 956–165 969, 2025.